Hyperspectral Modeling of Skin Appearance

TENN F. CHEN, GLADIMIR V. G. BARANOSKI, BRADLEY W. KIMMEL, and ERIK MIRANDA
University of Waterloo

Exploration of the hyperspectral domain offers a host of new research and application possibilities involving material appearance modeling. In this article, we address these prospects with respect to human skin, one of the most ubiquitous materials portrayed in synthetic imaging. We present the first hyperspectral model designed for the predictive rendering of skin appearance attributes in the ultraviolet, visible, and infrared domains. The proposed model incorporates the intrinsic bio-optical properties of human skin affecting light transport in these spectral regions, including the particle nature and distribution patterns of the main light attenuation agents found within the cutaneous tissues. Accordingly, it accounts for phenomena that significantly affect skin spectral signatures, both within and outside the visible domain, such as detour and sieve effects, that are overlooked by existing skin appearance models. Using a first-principles approach, the proposed model computes the surface and subsurface scattering components of skin reflectance taking into account not only the wavelength and the illumination geometry, but also the positional dependence of the reflected light. Hence, the spectral and spatial distributions of light interacting with human skin can be comprehensively represented in terms of hyperspectral reflectance and BSSRDF, respectively.

Categories and Subject Descriptors: I.3.7 [**Computer Graphics**]: Three-Dimensional Graphics and Realism—*Raytracing*

General Terms: Algorithms

Additional Key Words and Phrases: Material appearance modeling, light transport, rendering, hyperspectral imaging, visualization

ACM Reference Format:

Tenn F. Chen, Gladimir V. G. Baranoski, Bradley W. Kimmel, and Erik Miranda. 2015. Hyperspectral modeling of skin appearance. ACM Trans. Graph. 34, 3. Article 31 (April 2015), 14 pages.
DOI: http://dx.doi.org/10.1145/2701416

1. INTRODUCTION

Despite significant advances achieved by the computer graphics community with respect to the modeling of material appearance, organic materials such as human skin continue to represent an ongoing challenge in this area due to their inherent optical complexity. Moreover, to date, the bulk of the work on light and skin interactions within the computer graphics field has been aimed at skin imaging in the visible domain. In fact, only recently have computer graphics researchers started to look more closely into the hyperspectral domain, spanning from the ultraviolet (UV) to the infrared (IR) regions of the light spectrum, in order to broaden the scope of traditional rendering frameworks [Kim et al. 2012]. Accordingly, existing skin appearance models have been primarily employed in image synthesis applications (e.g., Donner et al. [2008] and Jimenez et al. [2010]) as well as in biomedical investigations (e.g., Baranoski et al. [2012a] and Cavalcanti et al. [2013]) centered on the visible appearance attributes of human skin. However, there are relevant avenues of research associated with skin appearance modeling that remain unexplored, notably involving the hyperspectral simulation of light and skin interactions and the modeling of aging and weathering phenomena, a forefront topic in the pursuit of realism [Dorsey et al. 2007; Mérillou and Ghazanfarpour 2008]. For example, many skin appearance changes distinctly noticeable in the visible domain are caused by natural processes, such as tanning [Chedekel 1995], freckling [Fulton 1997], and photoaging [Schroeder et al. 2008] triggered by exposure to UV and IR light. In order to predictively simulate these processes, it is necessary in turn to employ models that can correctly account for light and skin interactions, both within and outside the visible domain.

The investigation and rendering of phenomena affecting skin appearance attributes within a broader hyperspectral domain can also lead to a diverse scope of applications in the life and health sciences. For example, the presence of pigmentation irregularities such as freckles, moles, and other forms of melanin clumping is accentuated in the UV domain (Figure 2 (left)). Predictive images depicting this phenomenon can be employed in appearance-based interventions aiming at increasing the willingness of individuals to adopt sun protection measures that can reduce photodamage effects and skin cancer risk [Mahler et al. 2003]. In addition, the modeling of skin hyperspectral responses can be utilized in noninvasive health monitoring procedures of relevance for medical and cosmetics research as well as clinical practice. For example, UV responses can be used in the assessment of the intrinsic photoprotective properties of a skin specimen [Nielsen et al. 2004], while IR responses can be used in the assessment of skin hydration [Attas et al. 2002], a key factor contributing to skin health.

Hyperspectral modeling of skin appearance also offers a myriad of creative opportunities for aesthetic applications. For example, in the IR region, notably below 1300nm, one can observe a "soft", more diffuse skin appearance (Figure 2 (right)) that is also less influenced by pigmentation irregularities [Anderson and Parrish 1982; Fredembach et al. 2009]. Unique, artistic images of human subjects can be obtained by eliciting this "ethereal" appearance of skin under IR light [Sandidge 2009].

There is a considerable amount of research on the simulation of light and skin interactions being performed in fields as diverse as colorimetry (e.g., Tsumura et al. [2000]), remote sensing (e.g., Nunez [2009]), and tissue optics (e.g., Prahl [1988]). It is worth noting, however, that the models proposed in these fields are

This research was supported by NSERC Discovery Grant no. 238337 and by scholarships from OGS and the University of Waterloo.
Authors' addresses: T. F. Chen (corresponding author), G. V. G. Baranoski, B. W. Kimmel, and E. Miranda, University of Waterloo, 200 University Avenue West, Waterloo, ON N2L 3G1, Canada; email: t4chen@uwaterloo.ca.

DOI: http://dx.doi.org/10.1145/2701416

Fig. 1. Images showing distinct skin appearance features in the ultraviolet (left), visible (center), and infrared (right) spectral domains. These images were rendered using BSSRDF (top row) and BRDF (bottom row) representations of spatial light distributions provided by the proposed hyperspectral model HyLIoS (*H*yperspectral *L*ight *I*mpingement *o*n *S*kin) in these domains. Note that HyLIoS can predictively simulate not only the intensification of pigmentation irregularities in the ultraviolet range, but also the "soft", "ethereal" (more diffuse and less affected by the presence of pigmentation irregularities) appearance of human skin in the infrared range [Sandidge 2009], notably below 1300nm [Anderson and Parrish 1982]. The ultraviolet and infrared responses (at 365nm and 1100nm, respectively) are depicted using pseudocolor.

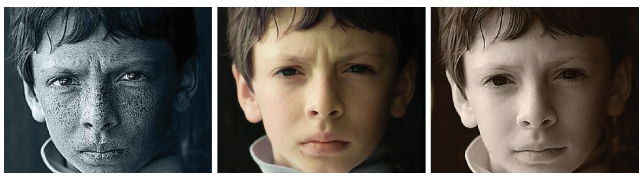

Fig. 2. Photos taken with a Nikon D2X camera equipped with different light transmitting filters. Left: UV filter. Center: no filter. Right: IR filter. Note the intensification of pigmentation irregularities in the UV range (employed in appearance-based cancer prevention initiatives [Mahler et al. 2003; Fulton 1997]), and the more diffuse, "ethereal" skin appearance that can be obtained in the IR domain (employed in artistic applications [Sandidge 2009]). The UV and IR photos are depicted using pseudocolor. Photos courtesy of Charles Schmitt.

not designed for the comprehensive simulation of material appearance within image synthesis frameworks, which involves both the spectral and spatial distributions of light interacting with a given material [Hunter and Harold 1987]. Instead, these models are primarily designed for specialized applications such as the detection and analysis of skin spectral signatures within specific regions of the light spectrum (e.g., Nielsen et al. [2004]).

In this article, we present the first hyperspectral skin appearance model, henceforth referred to as HyLIoS (*H*yperspectral *L*ight *I*mpingement *o*n *S*kin), capable of predictively simulating both the spectral and spatial distributions of light interacting with this complex biological material in the UV, visible, and IR domains, from 250–2500nm. The first-principles approach used in the design of the proposed model takes into account not only the detailed layered structure of the skin tissues, but also the particle nature of its main light attenuation agents, namely the melanosomes (spheroidal melanin-containing organelles [Olson et al. 1973]). Instead of relying on Mie-theory-based approximations in which light attenuation agents are usually represented by uniformly distributed spheres, we probabilistically incorporate the melanosomes' size, shape, orientation, and distribution into our light transport simulations. These also account for the hyperspectral absorption and scattering properties of the remaining light attenuation agents found in each layer. As a result, the proposed model can predictively account for phenomena that significantly affect skin spectral responses both within and outside the visible domain, such as light detour and sieve effects [Butler 1964; Latimer 1984], as well as the positional dependence [Nicodemus et al. 1992] of light interacting with a given skin specimen.

As highlighted by Greenberg et al. [1997], the evaluation of predictive simulations should involve comparison of their results with physical measurements whenever such data is available. Accordingly, the predictions of the proposed model are primarily evaluated through quantitative comparisons with measured data and qualitative comparisons with empirical observations reported in the literature. In addition, images rendered using the proposed model are employed to further illustrate its predictive capabilities with respect to the simulation of characteristic trends in the variation of skin appearance attributes, both within and outside the visible domain. Finally, practical issues related to its usability and performance are also examined in this article.

2. RELATED WORK

In this section, we briefly review key developments on the modeling of skin appearance within the computer graphics field. The reader interested in a more detailed examination of this body of work,

especially outside the computer graphics domain, is referred to comprehensive texts on this topic [Tuchin 2007; Igarashi et al. 2007; Baranoski and Krishnaswamy 2010].

Skin appearance models employed in realistic image synthesis can be broadly categorized into two groups: deterministic and nondeterministic. Deterministic models (e.g., Stam [2001], Donner and Jensen [2006], and Weyrich et al. [2006]) simulate the light and skin interactions using formulations based on analytical approximations to the radiative transfer equation such as the Kubelka-Munk theory, the diffusion theory, and the discrete-ordinate approximation [Igarashi et al. 2007; Baranoski and Krishnaswamy 2010]. Nondeterministic models (e.g., Hanrahan and Krueger [1993], Ng and Li [2001], and Krishnaswamy and Baranoski [2004a]) simulate these interactions using stochastic techniques based on Monte Carlo methods [Prahl 1988].

Deterministic models are faster and amenable to analytical manipulation, which favors their use in real-time applications aimed at generating believable images of virtual characters. However, it is important to note that the predictive capabilities of these models are bound by the inherent limitations of the analytical approximations employed in their formulations. For example, it has been demonstrated [Hielscher et al. 1995; Chen et al. 2001] that the diffusion theory approximation fails to accurately describe light propagation in highly absorbing media. In the case of human skin, strong absorption is verified in the UV, visible (below $\approx$ 600nm), and IR (above $\approx$ 1300nm) domains [Anderson and Parrish 1982]. Recently, algorithms have been proposed to relax the limitations of the diffusion theory approximation [d'Eon and Irving 2011]. These algorithms have been evaluated through comparisons with results provided by general-purpose Monte Carlo simulations [Wang et al. 1995] involving the reflectance and transmittance profiles within single- and two-layer homogeneous materials.

Nondeterministic models allow for the proper modeling of complex geometries and optical inhomogeneities [Prahl 1988; Hielscher et al. 1995; Wang et al. 1995], thus supporting utilization of first-principles simulation approaches. These approaches in turn apply fundamental principles of physics to a material's microscopic structure in order to build up the bulk behavior of how it interacts with light [Dorsey et al. 2007]. Accordingly, depending on the level of abstraction employed in the characterization of the skin specimens, they can lead to high-fidelity results. These models, however, are bound to incur higher processing times due to their use of Monte Carlo methods. For this reason, parallel processing strategies (e.g., Krishnaswamy and Baranoski [2004b]) and specialized graphics hardware (e.g., Doronin and Meglinski [2011]) are often employed to improve their performance.

Existing skin appearance models, either deterministic or nondeterministic, are not designed for providing predictive spectral responses with respect to a broader spectral domain, from UV to IR. For instance, it has been established [Anderson and Parrish 1982; Nielsen et al. 2006] that the effects of melanin on skin color and UV light attenuation must be related not only to melanin content, but also to where it is found and how it is dispersed within the cutaneous tissues. None of the existing skin appearance models accounts for the particle nature and distribution of melanosomes within the different epidermal layers, which impairs their predictive capabilities even in the visible domain as further discussed in Section 5. In addition, to the best of our knowledge, existing models do not account for the presence and distribution of other major contributors to light attenuation outside the visible domain such as keratin, DNA, urocanic acid, water, and lipids [Young 1997; Yang et al. 2009].

It is worth mentioning that there have been relevant computer graphics works involving the measurement of skin spectral responses and the capture of skin appearance data (e.g., Marschner et al. [1999], Fuchs et al. [2005], Weyrich et al. [2006], Donner et al. [2008], and Ghosh et al. [2008]). These efforts, however, were also aimed at applications in the visible domain and consequently primarily targeted the acquisition of skin appearance data in this region of the light spectrum.

3. BIOPHYSICAL BACKGROUND

In order to predictively model the appearance attributes of human skin, it is necessary to account for its intrinsic bio-optical properties. Although previous work in this area has examined these properties, for completeness we briefly review it from a hyperspectral perspective in this section.

Human skin is usually described as being composed of three distinct tissues, namely stratum corneum, epidermis, and dermis [Yang et al. 2009]. The stratum corneum and the epidermal layers (stratum lucidum, stratum granulosum, stratum spinosum, and stratum basale, from outermost to innermost) are composed of stratified cells with a combined thickness that may reach about 1mm [Anderson and Parrish 1982; de Graaff 1995]. Note that the stratum lucidum is a clear layer found only in thick skin regions such as palms and soles [de Graaff 1995] and for these reasons not further addressed in this work. The dermis can be divided into the outermost papillary dermis and innermost reticular dermis, with a combined thickness that may reach up to 4mm [Anderson and Parrish 1982]. Compared to the reticular dermis, the papillary dermis is relatively thin and contains smaller-sized structural fibers. The dermis also contains a network of blood vessels, with wider vessels being located in the reticular dermis.

Light impinging on the skin surface can be reflected back to the environment or transmitted into its internal tissues, a process that can be described in terms of the Fresnel equations [Anderson and Parrish 1982]. Once light is transmitted into the skin tissues, it can be absorbed or scattered by their constituent materials. In the remainder of this section, we outline the most important of these attenuation agents contributing to light absorption and scattering within the cutaneous tissues in the UV, visible, and IR domains.

3.1 Light-Absorbing Materials

Relevant light-absorbing materials acting in the UV domain are situated within the stratum corneum and epidermis [Young 1997]. These include DNA, keratin, urocanic acid, and melanin, which may occur in two forms within human skin: the dominant brown-black eumelanin and the yellow-red pheomelanin [Chedekel 1995].

Melanin is also a strong absorber in the visible range [Anderson and Parrish 1982]. It is synthesized by melanocyte cells in the stratum basale, where it is preferentially concentrated [de Graaff 1995]. As the epidermal cells move upward, it is distributed throughout the full thickness of the upper layers [Kollias et al. 1991]. Melanin may occur in a colloidal form (also known as *melanin dust*) or clustered within the melanosomes [Pathak 1995], where its content may range from 17.9% to 72.3% [Kollias et al. 1991].

Blood-borne pigments (e.g., oxyhemoglobin, deoxyhemoglobin, carboxyhemoglobin, methemoglobin, sulfhemoglobin, bilirubin and beta-carotene) found in the dermis are also relevant absorbers in the UV and visible domains [Jacquez et al. 1955b]. It is worth noting that beta-carotene may be also found in the epidermis and stratum corneum [Anderson and Parrish 1982]. Water and lipids found throughout the skin dominate the absorption of light in the IR domain [Jacquez et al. 1955a; Cooksey and Allen 2013], notably within the thick dermis [Yang et al. 2009].

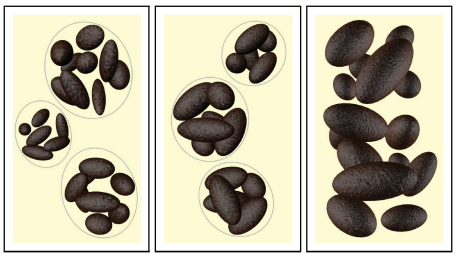

Fig. 3. Sketches depicting the distribution of melanosomes within the epidermal layers of skin specimens with different levels of melanin pigmentation. Left: melanosome complexes found in lightly pigmented specimens. Center: more compact complexes found in moderately pigmented specimens. Right: individually dispersed melanosomes found in darkly pigmented specimens.

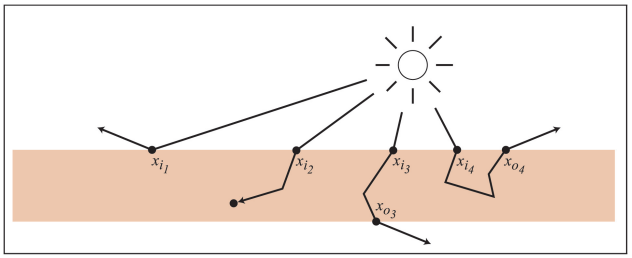

Fig. 4. Sketch illustrating the different light and skin interaction processes simulated by the proposed hyperspectral model (HyLIoS). From left to right: surface reflection, absorption, transmission, and subsurface reflection. Note that the distances that may separate light incidence (x_i) and outgoing (x_o) points are computed taking into account the physical distances that light travels within the cutaneous tissues.

Stratum corneum		UV
Epidermis	Stratum granulosum	UV-Vis
	Stratum spinosum	UV-Vis
	Stratum basale	UV-Vis
Dermis	Papillary dermis	Vis-IR
	Reticular dermis	Vis-IR

Fig. 5. Diagram showing the skin layers considered by the proposed hyperspectral model (HyLIoS). The main light-absorbing spectral domains associated with each layer are identified as UV (UltraViolet), Vis (Visible), and IR (InfraRed).

3.2 Light-Scattering Materials

Light is mostly scattered by heterogeneous structures, such as cells, organelles, and fibers, found within the skin tissues [Anderson and Parrish 1982]. Among these structures, the melanosomes, which predominantly scatter light in the forward direction [Chedekel 1995], have a central role in the attenuation of UV and visible light [Kollias et al. 1991]. The quantity of melanosomes produced in human skin is determined by genetic factors and sun exposure. In darkly pigmented specimens, the mean epidermal melanosome content (volume fraction) may be as high as 10%, while in lightly pigmented specimens may be as low as 1% [Lister 2013].

Melanosomes can be described as particles with the shape of a prolate spheroid [Olson et al. 1973]. In lightly pigmented specimens, they can occur in groups surrounded by a transparent membrane forming melanosome complexes [Szabo et al. 1969; Olson et al. 1973], which are characterized as approximately spherical in shape [Szabo et al. 1969; Kollias et al. 1991] (Figure 3 (left and center)). In darkly pigmented specimens, however, they occur as denser and individually dispersed particles [Szabo et al. 1969; Olson et al. 1973] (Figure 3 (right)).

The turbid dermal layers contain dense connective tissue. Light traversing these layers is subject to Rayleigh scattering, that may be caused by the presence of small-scale features, such as collagen fibers and fibrils, in the papillary dermis [Anderson and Parrish 1982; Jacques 1996]. Moreover, as light penetrates deeper into the dermal layers, it becomes progressively more diffuse [Jacques et al. 1987]. Eventually, the light traversing the dermis may reach the hypodermis. Light remission by large cellular structures in this adipose tissue can further contribute to an increase in the scattering of light within the dermis [Yang et al. 2009].

3.3 Detour and Sieve Effects

When light traverses a turbid medium, refractive index differences between pigment-containing structures and the surrounding medium may cause multiple interactions that increase the light optical path length, a phenomenon known as *detour effect* [Butler 1964]. Conversely, the traversing light may undergo a *sieve effect*, that is it may not encounter a pigment-containing structure [Latimer 1984]. While the former increases the probability of light absorption by the pigment of interest, notably in bands of absorption minima, in comparison with a homogeneous solution with equal concentration of this pigment [Butler 1964], the latter reduces the probability of light absorption, particularly in bands of absorption maxima [Latimer 1984]. The net result of these effects depends on the absorption spectra of the pigments as well as the distribution and volume fraction of the pigment-containing structures (e.g., melanosomes and melanosome complexes) found in a given medium [Butler 1964; Latimer 1984].

4. THE HYLIOS MODEL

The proposed model employs stochastic techniques to simulate the interactions of light with human skin. Using a first-principles approach, it accounts for the physical distances traveled by light within the cutaneous tissues. As a result, the radiometric responses derived from the light interaction processes affecting skin appearance can be quantified in terms of BSSRDF (bidirectional scattering-surface reflectance-distribution function) since the distances that may separate the light incidence (x_i) and outgoing (x_o) points (Figure 4) are provided by the simulations. Alternatively, these radiometric responses can be quantified in terms of BRDF (bidirectional reflectance-distribution function) by ignoring this positional parameter [Nicodemus et al. 1992].

Within the proposed modeling framework, the main cutaneous tissues, namely stratum corneum, stratum granulosum, stratum spinosum, stratum basale, papillary dermis, and reticular dermis, are represented by semi-infinite layers as depicted in Figure 5. These layers are characterized by their thickness refractive index as well as the presence and optical properties of light attenuation materials.

The propagation and attenuation of light within the various skin layers are simulated through an iterative random walk algorithm which is schematically presented in Figure 6. Within this simulation framework, absorbers represent materials that primarily

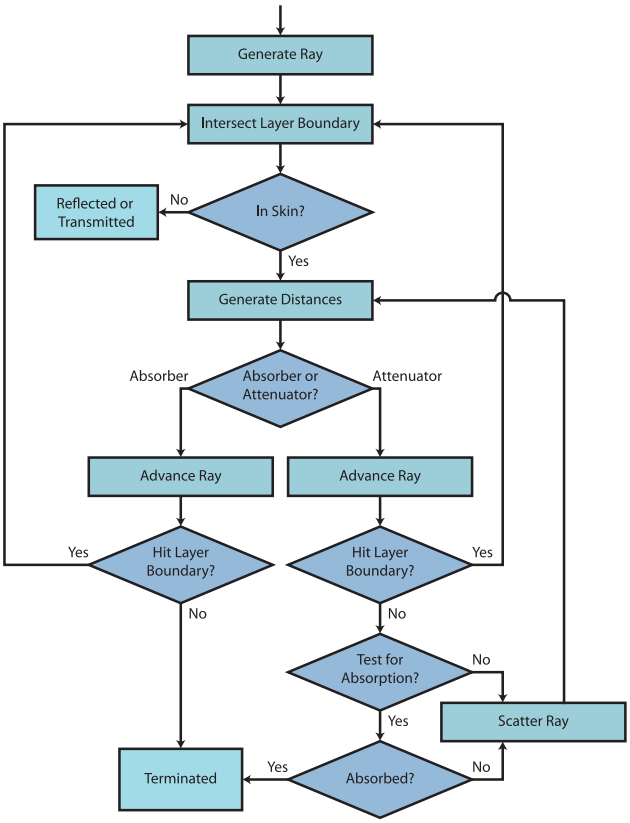

Fig. 6. Flowchart depicting the general structure of the iterative random walk algorithm employed by the proposed hyperspectral model (HyLIoS). The distances to the next attenuation events are computed using Eq. (1).

absorb light, while attenuators represent materials that primarily scatter light (e.g., connective fibers) as well as materials that significantly contribute to both absorption and scattering of light (e.g., melanosomes). Although light is represented by discrete rays, each one associated with a given wavelength λ, the attenuation events are probabilistically accounted for using ray optics and, when appropriate, data-driven procedures based on wave optics observations.

At the start of each iteration, a Fresnel test is performed when a ray hits a layer interface. If the ray exits the skin, a reflection or transmission event is recorded and the iteration terminated. Otherwise, the distance to the next attenuation event is probabilistically computed as follows. When a ray travels through a layer, it may interact with various absorbers and attenuators. Each of these tissue constituents may be associated with a different spectral attenuation coefficient $\mu(\lambda)$. For each relevant $\mu(\lambda)$, we generate a distance $d(\lambda)$ [Prahl 1988] given by

$$d(\lambda) = -\frac{1}{\mu(\lambda)} \ln \xi_1, \tag{1}$$

where ξ_1 is a random number uniformly generated from (0, 1]. The actual distance travelled by the ray to the next attenuation event corresponds to the smallest of these generated distances, that is, we advance the ray by this distance. If the ray hits a layer interface, the process reiterates from the Fresnel test; otherwise, three possible outcomes may take place (Figure 6). In the case of absorbers, the ray is terminated. In the case of attenuators that can significantly contribute to both absorption and scattering, a probabilistic test (Section 4.2.1) is used to determine whether the ray is absorbed. If the test fails, the ray is scattered (Section 4.2.1) and the random walk continues; otherwise, the ray is terminated. In the case of attenuators that primarily scatter light, the ray is scattered (Section 4.2.2) and the random walk proceeds.

In the following sections, we describe how the light attenuation contributions of absorbers, attenuators, and large-scale cellular structures are accounted for in the algorithmic formulation of the proposed model.

4.1 Absorbers

In order to account for the contributions of the absorbers present in a given layer, we compute the spectral volumetric absorption coefficient associated with the layer, which corresponds to the weighted sum of the specific spectral absorption coefficients of each absorber. For example, the absorption in the papillary dermis is primarily due to water, lipids, and blood pigments. Let the blood-borne pigments oxyhemoglobin, deoxyhemoglobin, carboxyhemoglobin, methemoglobin, sulfhemoglobin, beta-carotene, and bilirubin be denoted by oh, dh, ch, mh, sh, bc, and bil, respectively. The corresponding volumetric absorption coefficient of the papillary dermis can then be calculated as

$$\begin{aligned}\mu_a^p(\lambda) \;=\; & \zeta_{water}(\lambda) v_{water}^p + \zeta_{lipids}(\lambda) v_{lipids}^p \\ & + (\zeta_{oh}(\lambda) v_{oh}^b + \zeta_{dh}(\lambda) v_{dh}^b + \zeta_{ch}(\lambda) v_{sh}^b \\ & + \zeta_{mh}(\lambda) v_{mh}^b + \zeta_{sh}(\lambda) v_{sh}^b \\ & + \zeta_{bc}(\lambda) v_{bc}^b + \zeta_{bil}(\lambda) v_{bil}^b) v_{blood}^p,\end{aligned} \tag{2}$$

where ζ_i, v_i^p, and v_i^b correspond respectively to the specific absorption coefficient of a given absorber i, its volume fraction within the papillary dermis, and its volume fraction within whole blood.

Recall that melanin may be found dispersed in a colloidal form or clustered within the melanosomes (Section 3.1). In the former case, its specific absorption coefficients (for eumelanin and pheomelanin) are aggregated to the specific absorption coefficients of the pigments found in a given layer as described earlier. In the latter case, the computation of its attenuation coefficient takes into account its concentration within each individual melanosome. This coefficient is then employed in the absorption tests performed considering the specific geometrical and optical characteristics of these melanin-containing organelles (Section 4.2.1).

4.2 Attenuators

Melanosomes and connective fibers are incorporated into the proposed model as attenuators. Based on experimental investigations [Latimer 1984], the perturbations caused by these materials on the propagated light are assumed azimuthally symmetric. Accordingly, the corresponding azimuthal angle of perturbation is uniformly sampled from $[0, 2\pi)$.

4.2.1 *Melanosomes and Melanosome Complexes.* Individually dispersed melanosomes (in darkly pigmented specimens) and melanosome complexes (in lightly and moderately pigmented specimens) are probabilistically generated, positioned, and oriented on-the-fly in a given epidermal layer (Figure 7). This approach enables the simulation of light interactions with each melanosome without having to explicitly store these organelles, as well as avoiding expensive ray-melanosome intersection tests.

Melanosomes are modeled as prolate spheroids employing dimensions reported in the literature [Olson et al. 1973], while

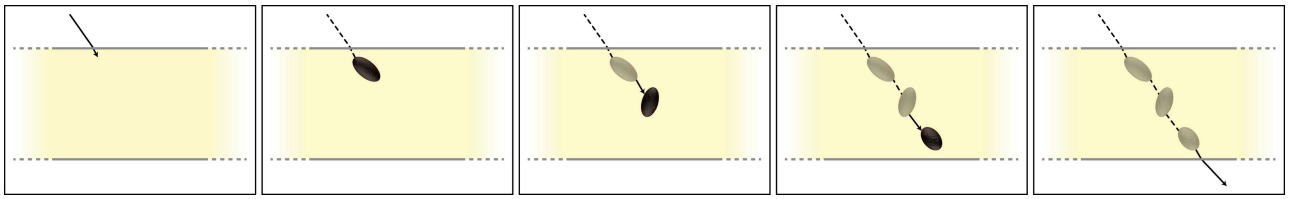

Fig. 7. Diagram illustrating a possible path (from left to right) that can be followed by a ray traversing an epidermal layer occupied by individual melanosomes (represented by prolate spheroids). The distance to the next melanosome is probabilistically computed according to a path-length distribution. The orientation of the melanosome as well as a hitting point on its surface are also probabilistically generated. The light interaction with the melanosome is simulated, and the ray is either terminated inside the melanosome or scattered. In the latter case, the melanosome is discarded and a new one generated. This process is repeated until the ray is either absorbed or scattered outside of the layer. The same stochastic procedure is employed for melanosome complexes.

melanosome complexes are modeled as spheres [Kollias et al. 1991]. Based on experimental observations [Szabo et al. 1969], for lightly pigmented specimens the sphere diameter is set to be twice the major axis of the spheroids representing the encapsulated melanosomes. Similarly, for moderately pigmented specimens this diameter is set to be equal to the major axis of the spheroids [Szabo et al. 1969].

The attenuation coefficient of a melanosome is given by its geometric attenuation coefficient [Kimmel and Baranoski 2007]

$$\mu_g = \frac{S}{V}\frac{v}{4}, \tag{3}$$

where S is the surface area, V the volume, and v the volume fraction. The ratio S/V for a prolate spheroid is calculated as

$$\frac{S}{V} = \frac{3}{2a}\left(\frac{a}{b} + \frac{\arcsin c}{c}\right), \tag{4}$$

where a and b correspond to the lengths of the semi-minor and semi-major axes, respectively, and $c = \sqrt{(1 - a^2/b^2)}$.

Once the distance d is computed by substituting μ_g into Eq. (1), the orientation of the prolate spheroid is selected by sampling the Probability Distribution Functions (PDFs) associated with the orientation that was considered while generating the distance. These PDFs [Yim et al. 2012] are given by

$$P_m(\alpha) = \frac{\chi_1(1 - |\cos\alpha|) + \chi_2|\cos\alpha|}{\chi_1 + \chi_2}, \tag{5}$$

$$P_m(\beta) = \frac{1}{2\pi}, \tag{6}$$

where α and β correspond, respectively, to the polar and azimuthal angles defining the ray direction, and χ_1 and χ_2 correspond to the cross-sectional areas of the spheroid associated with its minor and major axes, respectively. Note that if the spheroid overlaps its predecessor, it is rejected and another one generated. Similarly, the spheroid is also rejected if it crosses a layer boundary. Finally, the hitting point on the spheroid surface is randomly selected among the set of points facing the ray, that is, by uniformly selecting a random point from the spheroid's projected surface facing the ray.

After the position, orientation, and hitting point are selected, the model simulates the light-melanosome interactions taking into account the dual photon-wave nature of these interactions. As observed by Latimer [1984], when light traverses an organelle, the light waves tend to reach out and interact with parts of the organelle that are geometrically outside their straight-line path, resulting in an absorption enhancement. In order to account for this absorption enhancement, the ray traversing the melanosome is tested for absorption considering the possibility of multiple internal interactions as described next. The distance that the ray can travel until the next attenuation event is computed employing Eq. (1) and using the aggregated specific absorption coefficients of eumelanin and pheomelanin as the corresponding attenuation coefficient (Section 4.1). If this distance does not allow the ray to exit the melanosome, the ray is terminated, otherwise, a Fresnel test is performed to determine whether the ray is transmitted out of or bounced inside the spheroid due to the refractive index difference between the clustered melanin and the surrounding medium (epidermal tissue). When the ray is bounced, it is diffusely perturbed to account for the irregular morphology of the different melanosome parts [Kollias et al. 1991] subjected to the light-organelle interactions [Latimer 1984] mentioned earlier. Accordingly, the polar perturbation angle is sampled from $[0, \pi/2)$ using a PDF based on the cosine distribution, that is, the polar perturbation angle is given by $\arccos(\sqrt{1 - \xi_2})$, where ξ_2 represents a random number uniformly sampled from [0,1). Rejection sampling is employed to guarantee that the perturbed ray, denoted by $\vec{r}_p$, remains inside the melanosome, that is, if $\vec{r}_p \cdot \vec{n} < 0$, where $\vec{n}$ corresponds to the inward normal at the intersection point, the ray is rejected. In this case, another perturbed ray is obtained and the rejection test repeated. After applying this perturbation procedure, the process inside the melanosome reiterates from the absorption test.

In the case of the melanosome complexes, their attenuation coefficient is also obtained using Eq. (3), with the ratio S/V given by $3/r_s$ [Kimmel and Baranoski 2007], where r_s is the radius of the corresponding sphere. When a ray encounters a melanosome complex, it interacts with at most n_m encapsulated melanosomes, where n_m corresponds to the ratio of the diameter of the encapsulating sphere to the minor axis of the spheroid representing the melanosomes [Szabo et al. 1969]. Each of these interactions will involve the melanosome orientation selection and the absorption test described before.

If a ray is not absorbed by an individually dispersed melanosome or a melanosome complex, it is scattered. The forward scattering behavior of the melanosomes [Chedekel 1995] is simulated using a data-driven procedure that also follows the dual photon-wave nature of the light-organelle interactions [Latimer 1984] mentioned earlier. More specifically, the corresponding polar scattering angle θ_m is sampled from an exponential distribution that has a mean angle $\theta_\circ$. This mean angle was selected to be 5° based on wave optics experimental observations on the scattering behavior of pigment-containing organelles [Latimer 1984]. Furthermore, since light-melanosome interactions have an increasingly diminished contribution to light attenuation from 780nm–1300nm, being essentially negligible beyond $\approx$ 1400nm [Anderson and Parrish 1982], we linearly reduce $\theta_\circ$ to 0 over this region. Accordingly, the polar angle θ_m is generated using Algorithm 1, where ξ_3 and ξ_4 are random numbers uniformly sampled from [0, 1). Similarly, in

the case of a melanosome complex, Algorithm 1 is applied if all encapsulated melanosomes fail the absorption test.

ALGORITHM 1: Exponential perturbation (mean angle $\theta_\circ$)

$\phi = \arctan(\theta_\circ)$
$max = (1/\theta_\circ) \times \exp(-\phi/\theta_\circ) \times \sin(\phi)$
repeat
  $\xi_3, \xi_4 = random[0, 1)$
  $\theta_m = \pi\xi_3$
until $max \times \xi_4 \leq (1/\theta_\circ) \times \exp(-\theta_m/\theta_\circ) \times \sin(\theta_m)$
return θ_m

4.2.2 *Connective Fibers.* It has been proposed [Jacques 1996] that the scattering caused by the thin connective fibers in the papillary dermis follows the Rayleigh scattering formulation. Hence, the attenuation coefficient associated with these fibers is calculated using the following expression [McCartney 1976] for the Rayleigh scattering coefficient:

$$\mu_s^R(\lambda) = \frac{128\pi^5 r^6 v_f}{3\lambda^4} \left(\frac{4}{3}\pi r^3\right)^{-1} \left(\frac{\eta^2 - 1}{\eta^2 + 1}\right)^2, \quad (7)$$

where r and v_f represent the radius and the volume fraction occupied by the connective fibers, respectively, and η corresponds to the ratio between the refractive index of these scatterers to the refractive index of their surrounding medium. Based on data provided by Jacques [1996], we consider $r = 100$nm, $\eta = 1.5/1.33$, and $v_f = 0.22$ as default values in our simulations.

The ray direction of propagation is perturbed considering the Rayleigh scattering distribution [McCartney 1976]. Accordingly, the polar angle θ_R is generated using Algorithm 2, where ξ_5 and ξ_6 are random numbers uniformly sampled from [0, 1). Since the attenuation coefficient computed for these materials describes bulk scattering, the contributions of these attenuators are taken into account only once per ray pass through the papillary dermis.

ALGORITHM 2: Rayleigh perturbation

repeat
  $\xi_5, \xi_6 = random[0, 1)$
  $\theta_R = \pi\xi_5$
until $\xi_6 \leq \left(\frac{3\sqrt{6}}{8}\right)(1 + \cos^2\theta_R)\sin\theta_R$
return θ_R

4.3 Large-Scale Cellular Structures

A portion of the light that interacts with the skin surface (stratum corneum) cells may be reflected back to the environment following the execution of a Fresnel test [Anderson and Parrish 1982]. To account for the influence of the skin surface roughness on the distribution of the reflected rays, the surface normals are perturbed using a procedure based on the Trowbridge-Reitz function [Trowbridge and Reitz 1975] that represents rough air-cell interfaces using randomly curved microareas. Accordingly, when a ray impinges on the skin surface, the azimuthal angle of the perturbed surface normal is uniformly sampled from $[0, 2\pi)$, while the polar angle θ_s is generated using the following distribution:

$$P_s(\theta_s) = \frac{s^4}{(s^2\cos^2\theta_s + \sin^2\theta_s)^2}\sin\theta_s, \quad (8)$$

where s is the roughness parameter associated with the aspect ratio of the stratum corneum cells, that is, the flatter the cells (lower s), the closer the spatial distribution of reflected rays approaches a specular distribution.

Since the large cellular structures found in the hypodermis reflect most of the impinging light (Section 3.2), the dermal-hypodermal junction is set to have a reflectance equal to 1. In addition, considering that light becomes progressively more diffuse as it travels further within the dermis [Jacques et al. 1987], the rays reflected at the dermal-hypodermal junction are diffusely perturbed, that is, the azimuthal perturbation angle is uniformly sampled from $[0, 2\pi)$ and the polar perturbation angle is sampled from $[0, \pi/2)$ using the PDF based on the cosine distribution previously provided (Section 4.2.1).

5. RESULTS AND DISCUSSION

In order to evaluate the predictive capabilities of the proposed model, we have compared its results with measured data and experimental observations reported in the literature. In the absence of measured skin characterization data for the specimens used in the actual experiments, the values assigned to the pigmentation parameters employed in the computation of the HyLIoS modeled curves (Table I) were selected based on the specimens' original descriptions and the corresponding ranges for these parameters provided in related scientific work [Kollias et al. 1991; Jacques 1996; Hennessy et al. 2005; Lister 2013]. In order to account for melanosome degradation in the upper epidermal layers [Nielsen et al. 2006], the axes of the melanosomes located in the stratum spinosum and stratum granulosum were set, respectively, as 50% and 25% of the values (in $\mu m \times \mu m$) provided by Olson et al. [1973], namely 0.40×0.17 and 0.69×0.28 for lightly and darkly pigmented specimens, respectively.

For conserving space, the values selected for the remaining model parameters, such as the thickness, refractive index, and water content associated with each skin layer, are provided in a supplementary data file [Chen et al. 2014] along with the concentrations and absorption spectra of the absorbers employed in our simulations, which include all those cited in Section 3.1. In addition, we note that HyLIoS can be run online [Natural Phenomena Simulation Group (NPSG) 2014] via a model distribution system [Baranoski et al. 2012] that enables researchers to specify simulation conditions (e.g., angle of incidence and spectral range), modify specimen characterization parameters, and obtain modeled directional-hemispherical reflectance curves including those depicted in the quantitative comparisons presented in this work. Regarding the rendered images in the visible domain presented herein, unless otherwise stated, they were generated considering BSSRDF readings and light sources that approximate a standard D65 illuminant [Hunter and Harold 1987].

5.1 Quantitative and Qualitative Comparisons

Existing skin appearance models designed for applications in the visible domain, such as the diffusion-theory-based model proposed by Donner and Jensen [2006] (henceforth referred to as DJ06) and the stochastic model proposed by Krishnaswamy and Baranoski [2004a] (known as BioSpec), assume melanin to be uniformly distributed in a single layer representing the epidermis. Moreover, they take into account neither the particle nature nor the distribution patterns of the melanosomes (Section 3.2). These limitations preclude these models from accounting for detour and sieve effects (Section 3.3), which can lead to prominent discrepancies, notably

Table I. Main HyLIoS Pigmentation Parameters Used to Generate Reflectance Curves for Different Skin Specimens

Parameter	S1	S2	S3	S4
Epidermal Melanosome Content (%)	1.0, 1.0, 1.0	0.00, 0.00, 3.75	0.00, 0.00, 3.0	10.0, 10.0, 10.0
Epidermal Colloidal Melanin Content (%)	0.8	1.25	1.35	15.0
Melanosome Eumelanin Concentration (mg/mL)	90.0	50.0	32.0	50.0
Melanosome Pheomelanin Concentration (mg/mL)	4.0	2.0	2.0	4.0
Papillary Dermis Blood Content (%)	0.2	0.7	0.3	2.5
Reticular Dermis Blood Content (%)	0.2	0.7	0.3	2.5

The triples given in the top row correspond to values assigned to the three epidermal strata: granulosum, spinosum, and basale, respectively. Note that the datasets S1, S2, and S3 correspond to specimens with relative low level of melanin pigmentation [Vrhel et al. 1994; Cooksey and Allen 2013], while dataset S4 corresponds to a specimen with a high level of melanin pigmentation [Jacquez et al. 1955a, 1955b]. Accordingly, the simulations consider the melanosomes distributed as complexes (Figure 3 (left)) when using datasets S1, S2, and S3, and as individually dispersed particles (Figure 3 (right)) when using dataset S4 [Szabo et al. 1969; Olson et al. 1973].

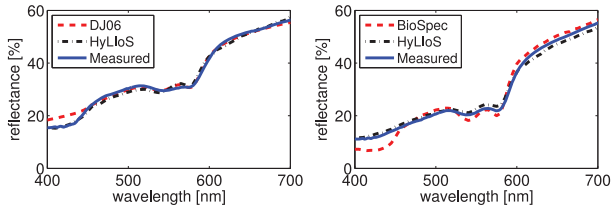

Fig. 8. Comparisons of modeled spectral curves obtained using DJ06 [Donner and Jensen 2006], BioSpec [Baranoski and Krishnaswamy 2010], and HyLIoS models with measured NCSU spectral curves 117 (left) and 113 (right) [Vrhel et al. 1994]. The HyLIoS curves on the left and right were computed using the pigmentation datasets S1 and S2, respectively (Table I).

Fig. 9. Skin swatches generated using modeled spectral curves provided by DJ06 (left) and HyLIoS (center) models along with a reference swatch (right) generated using measured data (NCSU spectral curve 117) provided by Vrhel et al. [1994]. The respective spectral curves are depicted in Figure 8 (left).

Fig. 10. Skin swatches generated using modeled spectral curves provided by BioSpec (left) and HyLIoS (center) models along with a reference swatch (right) generated using measured data (NCSU spectral curve 113) provided by Vrhel et al. [1994]. The respective spectral curves are depicted in Figure 8 (right).

in the blue end of the spectrum characterized by higher melanin absorption. Such discrepancies can be observed in the graphs presented in Figure 8. These graphs show comparisons of modeled results provided by DJ06, BioSpec, and HyLIoS with measured results provided by Vrhel et al. [1994] considering an angle of incidence of 45°, which are made available in a spectra database at the North Carolina State University (NCSU). In these comparisons, we employed NCSU curves used as references in the original evaluations of DJ06 and BioSpec. Note that the DJ06 modeled results depicted in Figure 8 were originally computed with the amount of eumelanin set to zero as reported by Donner and Jensen [2006]. Although this can mitigate the absorption-related limitations of the diffusion theory approximation outlined in Section 2, we remark that eumelanin is the dominant form of melanin present in human skin under normal physiological conditions [Anderson and Parrish 1982; Chedekel 1995; Hennessy et al. 2005; Kollias et al. 1991].

According to the trichromatic theory of color perception [Hunter and Harold 1987], the human eye's response to short-wavelength light stimulus is significantly less strong than its response to medium- and long-wavelength light stimuli. Since the previously mentioned discrepancies are located in the blue end of the visible spectrum, it is expected that they have a lower impact in the rendering of believable images of human skin. In order to illustrate this aspect, we have generated skin swatches using the data presented in Figure 8 (reflectance from 400–700nm with a resolution of 5nm) in conjunction with a standard XYZ-to-sRGB conversion procedure [Stone 2003]. As can be observed in the images depicted in Figures 9 and 10, despite these discrepancies, all three models can be effectively employed in the rendering of believable skin images. We remark, however, that the parameter values used in the computation of the BioSpec and HyLIoS curves depicted in Figure 8 were in closer agreement with the biophysical characteristics of skin specimens under normal physiological conditions, particularly with respect to eumelanin content.

The first-principles simulation approach employed by HyLIoS accounts not only for detour and sieve effects, but also for the strong forward scattering behavior of the epidermal layers, most notably in the UV domain [Bruls and van der Leun 1984] as shown in the plot presented in Figure 11. Recall that the particle nature and distribution patterns of the melanosomes have an even stronger influence on the skin spectral responses in the UV range [Anderson and Parrish 1982; Chedekel 1995], and the existing spectral models, different from HyLIoS, do not account for these factors. Hence, the simple incorporation of additional absorbers acting in the UV domain into these models would likely lead to discrepancies similar to those observed in the blue end of the visible spectrum (Figure 8).

In order to demonstrate the predictive capabilities of HyLIoS across the UV-visible-IR range, we compared modeled curves with measured curves provided by Cooksey and Allen [2013] and Jacquez et al. [1955a, 1955b] obtained for lightly and darkly pigmented skin specimens considering angles of incidence of 8° and 16.75°, respectively. As can be observed in the graphs provided in Figure 12, the relevant hyperspectral features (represented by the peaks and valleys) and trends are reproduced by the modeled

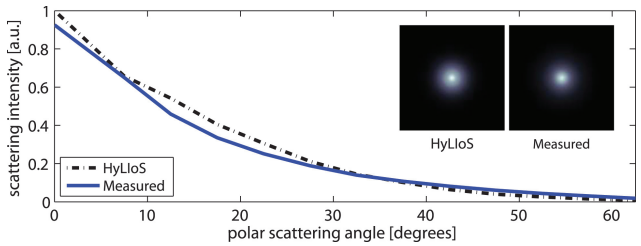

Fig. 11. Comparison of modeled subsurface scattering data obtained using HyLIoS with measured subsurface scattering data provided by Bruls and van der Leun [1984] for the epidermis of a lightly pigmented skin specimen considering normal incidence of UV light (at 302nm). The modeled data was computed using the pigmentation dataset S2 (Table I). The insets depict orthographic projections of the measured and modeled subsurface scattering data presented in the graph.

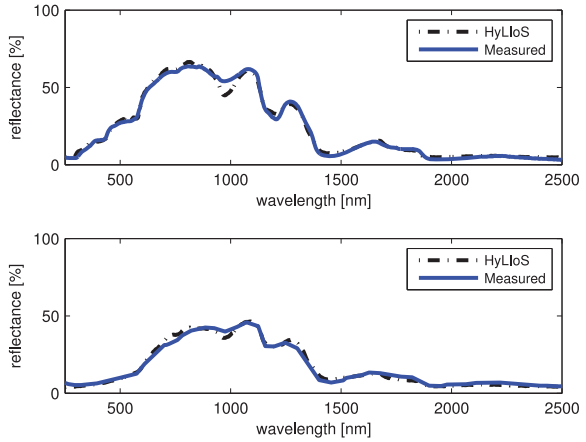

Fig. 12. Comparisons of modeled hyperspectral curves obtained using HyLIoS with measured curves for a lightly pigmented specimen (top) provided by Cooksey and Allen [2013] and a darkly pigmented specimen (bottom) provided by Jacquez et al. [1955a, 1955b]. The HyLIoS curves (from 250nm–2500nm) for the lightly and darkly pigmented specimens were computed using the pigmentation datasets S3 and S4, respectively (Table I).

curves. For example, for wavelengths longer than ≈1300nm, the absorption is dominated by the presence of water and lipids instead of melanin pigmentation [Anderson and Parrish 1982], resulting in a similarity between the measured reflectance spectra in this region. Such a similarity can also be observed between the modeled reflectance spectra. We note that localized quantitative variations can be expected across the UV-visible-IR domains since we employed, for both specimens, the same average values [Chen et al. 2014] for key characterization parameters such as the water content and the refractive index associated with each skin layer. As demonstrated by Cooksey and Allen [2013], population variability is the most significant source of uncertainty in the measurement of skin reflectance. We note, however, that our modeled results were obtained using parameter values within physiologically valid ranges indicated in the scientific literature.

We also examined the predictions of HyLIoS with respect to the spatial distribution of light. Although these predictions can be represented in terms of BSSRDF, we quantified them in terms of BRDF and integrated the resulting values over the visible domain to obtain BRDF curves that could be compared to the measured BRDF

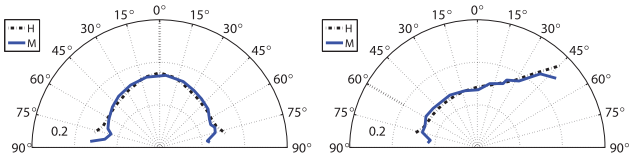

Fig. 13. Comparison of modeled BRDF curves (H) provided by HyLIoS with measured BRDF curves (M) provided by Marschner et at. [1999] for a lightly pigmented specimen considering two angles of incidence: 0° (left) and 60° (right). The modeled curves were obtained considering the pigmentation dataset S1 (Table I).

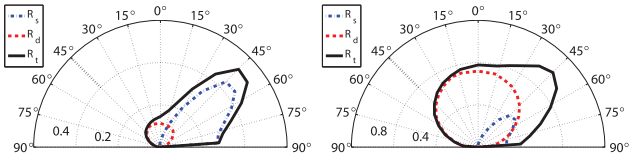

Fig. 14. Scattering plots provided by HyLIoS showing surface (R_s), subsurface (R_d), and total (R_t) reflectance distributions in the UV (left) and IR (right) domains. Note the more diffuse total reflectance distribution of IR light (below 1300nm) as reported in the scientific literature [Anderson and Parrish 1982; Hansen et al. 2010]. These plots correspond to normalized bidirectional reflectance values at 365nm (left) and 1100nm (right) multiplied by the cosine of the reflection angle. The bidirectional reflectance values were computed considering an angle of incidence of 45° and using the pigmentation dataset S1 (Table I).

curves provided by Marschner et al. [1999]. As can be observed in the comparisons depicted in Figure 13, HyLIoS can capture the angular dependency of the spatial distribution of light interacting with human skin in the visible domain. Moreover, recall that IR light can penetrate deeper into the cutaneous tissues than can UV light [Anderson and Parrish 1982], and can reach the dermal layers where it becomes progressively more diffuse [Jacques et al. 1987]. As a result, the subsurface reflectance has a more dominant role in the IR domain, and the overall reflected IR light, notably in the region below 1300nm (less susceptible to water absorption), has a more diffuse distribution than does UV light [Anderson and Parrish 1982; Hansen et al. 2010]. The scattering plots presented in Figure 14 indicate that HyLIoS can capture these distinct spatial distribution patterns of UV and IR light interacting with human skin.

The images presented in Figure 1 further demonstrate that HyLIoS can capture the distinct scattering behaviors of human skin in the hyperspectral domain. For example, the subject's face shows a more specular (glossier) behavior under UV light and a more diffuse behavior under IR light (below 1300nm), which are consistent with observations reported in the scientific literature [Anderson and Parrish 1982; Hansen et al. 2010]. It can also be observed that, although a more compact BRDF representation may be sufficient to capture the scattering profile in the UV domain (Figure 1 (left)), it cannot fully describe the "soft", more diffuse "ethereal" skin appearance in the IR domain [Fredembach et al. 2009; Sandidge 2009] provided by a BSSRDF representation (Figure 1 (right)).

It has been observed that a progressive increase in the overall epidermal melanin content leads to a fast convergence to low reflectance values in the UV domain [Fulton 1997]. As demonstrated by the images presented in Figure 15, HyLIoS can reproduce this trend, moreover, these images are consistent with measurements showing practically identical reflectance responses for moderately

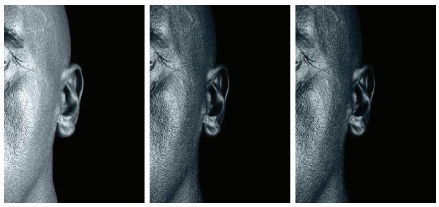

Fig. 15. Images showing the effects of increased overall melanin pigmentation on skin UV responses as reported in the scientific literature [Anderson and Parrish 1982; Cooksey and Allen 2013; Fulton 1997; Jacquez et al. 1955b; Nielsen et al. 2004]. Left: 1.5%. Center: 7%. Right: 30%. The UV responses (at 365nm) provided by HyLIoS are depicted in pseudocolor. Polygonal mesh courtesy of XYZ RGB, Inc.

Fig. 16. Images showing the magnifying effects of water loss on skin IR responses as reported in the scientific literature [Anderson and Parrish 1982; Attas et al. 2002]. These effects were simulated by reducing the water content of the cutaneous tissues of a lightly pigmented specimen (1.5% epidermal melanin content) within physiological limits [Blank 1952]. Left: no reduction. Center: 20% reduction. Right: 40% reduction. The IR responses (at 1650nm) provided by HyLIoS are depicted in pseudocolor. Polygonal mesh courtesy of XYZ RGB, Inc.

and darkly pigmented specimens in the UV domain [Jacquez et al. 1955b; Cooksey and Allen 2013].

Within the IR domain, the skin spectral responses are primarily determined by the absorption bands of water [Cooksey and Allen 2013; Jacquez et al. 1955a]. A myriad of physiological and environmental factors can alter the barrier activity of skin, thus intensifying water loss [Attas et al. 2002]. A reduction of water content in the cutaneous tissues Blank [1952] in turn results in an increase in reflectance in the IR domain [Anderson and Parrish 1982; Attas et al. 2002]. As shown by the images presented in Figure 16, this behavior is also captured by HyLIoS.

The presence of pigmentation irregularities, such as freckles and moles, is accentuated when a skin specimen is viewed under UV light due to the strong attenuation properties of melanin in this spectral domain [Pathak 1995; Fulton 1997]. This phenomenon is predictively simulated by HyLIoS as depicted in the images of a lightly pigmented individual (1.5% epidermal melanin content) presented in Figure 1. In these images, it can also be observed that the presence of these irregularities is less apparent in the IR domain, which is also consistent with empirical observations reported in the IR imaging literature [Fredembach et al. 2009; Sandidge 2009].

Due to the increasingly diminished contributions of melanin to light attenuation beyond 1100nm, the presence of pigmentation irregularities may become completely undetectable in this region dominated by water absorption [Anderson and Parrish 1982; Jacquez et al. 1955a]. In addition, the subsurface scattering contributions to skin reflectance tend to decrease due to the dominant role of water absorption, resulting in a more specular (glossier) and darker (lower reflectance) appearance of skin in this domain. As

Fig. 17. Images showing IR responses at 1200nm (left) and 1400nm (right) for a lightly pigmented specimen (1.5% epidermal melanin content). Note as reported in the scientific literature [Anderson and Parrish 1982; Jacquez et al. 1955a], the disappearance of pigmentation irregularities that occurs beyond 1100nm, as well as the more specular and darker appearance resulting from reduced subsurface scattering at a wavelength (1400nm) characterized by strong water absorption. Both (pseudocolor) images had their brightness increased for visualization purposes.

Table II. MSI Values Computed Considering the Complete Dataset S3 [Chen et al. 2014] as the Baseline and Its Modified Versions: No Melanin, No Blood, No DNA, No Keratin, No Water and No Lipids

	Removed Materials					
	Melanin	Blood	DNA	Keratin	Water	Lipids
MSI	0.415	0.229	0.135	0.068	0.611	0.026
SD	Vis	Vis	UV	UV	IR	IR
MSI_H	0.123	0.049	0.018	0.012	0.491	0.022

MSI values were computed for the spectral domain, denoted by "SD", in which the removal of each selected material has the highest impact. The MSI values computed considering the entire hyperspectral region of interest (250–2500nm), denoted by MSI_H, are also included for reference.

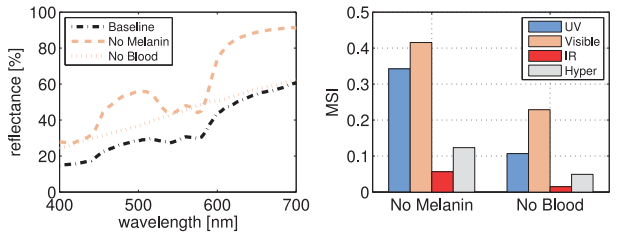

Fig. 18. Comparison of modeled results provided by HyLIoS depicting the impact of melanin and blood on skin reflectance, obtained considering the complete dataset S3 [Chen et al. 2014] as the baseline and two modified versions: with no melanin and no blood. Left: reflectance curves in the visible domain. Right: MSI values for each modified reflectance curve with respect to the baseline curve across the UV, visible, IR, and entire hyperspectral region of interest (250–2500nm) denoted by "Hyper".

demonstrated by the images presented Figure 17, these trends are also predictively reproduced by HyLIoS.

5.2 Input-Sensitivity Analysis

In the previous section, we have illustrated some of the effects that the main absorbers found within the cutaneous tissues have on modeled skin appearance attributes obtained using HyLIoS. Due to the different roles of these materials in the UV (250–400nm), visible (400–700nm) and IR (700–2500nm) regions of the light spectrum, it is expected that, for applications targeting a specific spectral domain, the parameters associated with a number of these materials may be kept fixed, that is, set to standard (average) values. In order to assess this possibility, we have performed an input-sensitivity

Fig. 19. Skin swatches illustrating the impact of melanin or blood removal on the visible appearance of human skin considering the complete dataset S3 [Chen et al. 2014] as baseline (left) and two modified versions: with no melanin (center) and no blood (right).

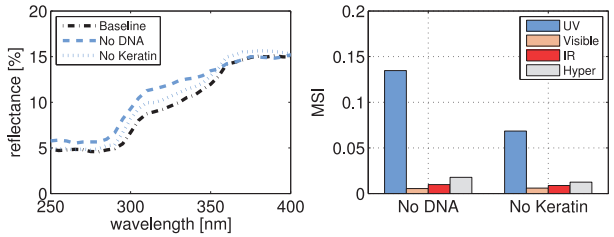

Fig. 20. Comparison of modeled results provided by HyLIoS depicting the impact of DNA and keratin on skin reflectance, obtained considering the complete dataset S3 [Chen et al. 2014] as the baseline and two modified versions: with no DNA and no keratin. Left: reflectance curves in the UV domain. Right: MSI values for each modified reflectance curve with respect to the baseline curve across the UV, visible, IR, and entire hyperspectral region of interest (250–2500nm) denoted by "Hyper".

Fig. 21. Skin swatches illustrating the impact of DNA or keratin removal on the UV appearance of human skin considering the complete dataset S3 [Chen et al. 2014] as baseline (left) and two modified versions: with no DNA (center) and no keratin (right). The UV responses are depicted in pseudocolor.

analysis Hamby [1994, 1995] in which we compared those obtained considering the complete dataset S3 [Chen et al. 2014] with those computed using modified versions of this dataset. These versions in turn account for the removal of specific materials, namely melanin, blood, DNA, keratin, water, and lipids. Note that we selected, without loss of generality, dataset S3 as baseline since its corresponding modeled reflectance curve (Figure 12 (top)) covers the entire hyperspectral region of interest. We also remark that this dataset is available at the HyLIoS Web site [Natural Phenomena Simulation Group (NPSG) 2014], which can be used to reproduce the results presented in this section by setting the parameters associated with a specific material to zero. The impact of each of the selected materials was quantified in terms of the mean sensitivity index Hamby [1994, 1995] expressed as

$$MSI = \frac{1}{N}\sum_{i=1}^{N}\frac{|\rho_b(\lambda_i) - \rho_m(\lambda_i)|}{\max\{\rho_b(\lambda_i),\, \rho_m(\lambda_i)\}}, \tag{9}$$

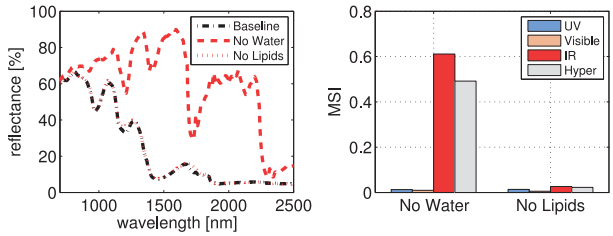

Fig. 22. Comparison of modeled results provided HyLIoS depicting the impact of water and lipids on skin reflectance, obtained considering the complete dataset S3 [Chen et al. 2014] as the baseline and two modified versions: with no water and no lipids. Left: reflectance curves in the IR domain. Right: MSI values for each modified reflectance curve with respect to the baseline curve across the UV, visible, IR, and entire hyperspectral region of interest (250–2500nm) denoted by "Hyper".

Fig. 23. Skin swatches illustrating the impact of water or lipids removal on the IR appearance of human skin considering the complete dataset S3 [Chen et al. 2014] as baseline (left) and two modified versions: with no water (center) and no lipids (right). The IR responses are depicted in pseudocolor.

Fig. 24. Rendered images illustrating changes in the visible appearance of human skin considering an increase in epidermal melanin content from 1.5% (left) to 7% (right). Note that we employed a back/side light source to make the translucency effects prominent. Polygonal mesh courtesy of XYZ RGB Inc.

where ρ_b and ρ_m correspond to the reflectances associated with the baseline and modified datasets, respectively, and N is the total number of wavelengths sampled with a 5nm resolution.

The overall results of our analysis presented in Table II show that melanin and water have the largest impact on the modeled reflectances. It is necessary to consider, however, that although a given material may not have a large impact in a certain spectral domain, it can still have a significant effect in the model's predictions. In order to demonstrate this aspect, we also present the results of our analysis grouped by materials that have their greatest impact in the visible, UV, and IR domains, respectively. These results in turn are further illustrated by skin swatches rendered using the corresponding modeled reflectances. The swatches depicting visible traits (Figure 19) were generated using the same approach employed in the rendering of the swatches depicted in Figures 9 and 10. The colors of the swatches in the UV and IR domains (Figures 20 and 22) were obtained by integrating the respective reflectance values

Fig. 25. Images illustrating rendering applications of HyLIoS in the UV (left), visible (center), and IR (right) spectral domains. The scene depicts an upper, back/shoulder (epidermal melanin content equal to 1.5%) with sunscreen and water in an outdoor beach setting. The UV and IR responses (at 365nm and 1650nm, respectively) are depicted using pseudocolor. The dark appearance of sunscreen and water outside the visible domain are attributed to their strong absorptive behavior in the UV and IR regions, respectively. Note that we have positioned the light source high above the subject in order to mimic a typical outdoor beach setting.

over the relevant spectral region and applying a tinted grayscale filter to the resulting values.

As can be observed in Figure 18 (left), the contributions of melanin and blood to skin appearance are prominent in the visible domain as the removal of either material significantly increases skin reflectance. Also, note that the characteristic omega shape observed in 500–600nm range vanishes with the removal of blood. These effects are reflected in the skin swatches (Figure 19), which depict a lighter appearance associated with the modified datasets. In addition, these materials have a significant impact outside the visible domain (Figure 18 (right)). Note that the baseline dataset corresponds to a lightly pigmented specimen, while specimens with higher melanin pigmentation levels, the dominant role of melanin is expected to be even more pronounced [Anderson and Parrish 1982].

Besides melanin and blood, other materials also have an impact, albeit not as pronounced, in the UV domain. For example, the removal of DNA or keratin yields higher reflectance (Figure 20 (left)), and results in a lighter UV appearance of skin (Figure 21). Although the removal of these materials affects other spectral regions, its effect is more significant in the UV domain (Figure 20 (right)).

The presence of water and lipids primarily affects the skin reflectance in the IR region, with water being the more dominant material (Figure 22 (left)). Accordingly, after water removal, skin appears significantly brighter in the IR domain (Figure 23). On the other hand, these materials have comparably negligible impact in the UV and visible domains (Figure 22 (left)).

In summary, for simulations aimed at believable rendering applications (Figures 24 and 25), the results presented in this section indicate that only the HyLIoS parameters associated with specific materials need to be modified in order to generate images of skin specimens with distinct appearance traits in a selected spectral region. For example, in the case of the visible domain dominated by melanin and blood, Table I provides the subset of parameters that can lead to the most significant skin appearance variations in this region. We note, however, that the HyLIoS detailed parameter space enables experimentation with a wider range of those biophysical factors associated with different physiological conditions affecting skin appearance. Such a capability is an asset for simulations aimed at broader applications in the life and health sciences.

5.3 Performance Issues

We observe that the current (CPU-based) implementation of HyLIoS is not particularly suitable for those real-time applications in the visible domain that demand results on the order of milliseconds. For example, it took $\approx 30s$ on a dual 6-core 2.66GHz Intel Xeon machine to obtain the 5nm resolution curves depicted in Figure 8 using 10^5 sample rays. Since several factors (e.g., image resolution, spectral sampling, and geometry) affect rendering time, it may take minutes or hours to generate an image, however, there are several hardware and software strategies that can be explored to enhance performance. For example, appearance attributes can be computed offline and quickly accessed on demand during the image generation process. We intend to explore such alternatives in our future work, as outlined in the next section.

6. CONCLUSION AND FUTURE WORK

In this article, we have described the first skin appearance model designed for the comprehensive simulation of spectral and spatial distributions of light interacting with human skin in the hyperspectral domain, from 250–2500nm. The proposed model represents the layered structure of the cutaneous tissues in more detail in comparison with existing skin appearance models, notably incorporating the particle nature and the different distribution patterns of the melanin-containing organelles. These features enable it to appropriately account for the positional dependence of skin reflectance as well as sieve and detour effects affecting light absorption within the cutaneous tissues.

By addressing the predictive modeling of skin appearance attributes in the hyperspectral domain, we aimed to contribute not only to the realistic rendering of human skin for entertainment, aesthetic, and educational purposes, but also for potential interdisciplinary applications such as the investigation of adverse effects of UV exposure and water loss on skin appearance. Accordingly, the predictive capabilities of the proposed model were evaluated primarily through comparisons with measured data and experimental observations reported in the scientific literature.

As future work, we plan to examine strategies for incorporating the proposed model into real-time rendering frameworks by exploiting specialized graphics hardware and numerical reconstruction approaches based on the use of principal component analysis and regression methods. In addition, we intend to address the simulation of phenomena such as skin fluorescence, in which the energy of different wavelengths is not decoupled (as opposed to the energy decoupling assumption traditionally employed in image synthesis).

ELECTRONIC APPENDIX

The electronic appendix to this article can be accessed in the ACM Digital Library.

REFERENCES

R. Anderson and J. Parrish. 1982. Optical properties of human skin. In *The Science of Photomedicine*, J. Regan and J. Parrish, Eds., Plenum Press, 147–194.

M. Attas, T. Posthumus, B. Schattka, M. Sowa, H. Mantsch, and S. Zhang. 2002. Long-wavelength near-infrared spectroscopic imaging for in-vivo skin hydration measurements. *Vibrat. Spectroscopy* 28, 37–43.

G. V. G. Baranoski, T. F. Chen, B. W. Kimmel, E. Miranda, and D. Yim. 2012. On the noninvasive optical monitoring and differentiation of methemoglobinemia and sulfhemoglobinemia. *J. Biomed. Optics* 17, 9, 097005–1–14.

G. V. G. Baranoski, T. Dimson, T. F. Chen, B. Kimmel, D. Yim, and E. Miranda. 2012. Rapid dissemination of light transport models on the Web. *IEEE Comput. Graph. Appl.* 32, 10–15.

G. V. G. Baranoski and A. Krishnaswamy. 2010. *Light and Skin Interactions: Simulations for Computer Graphics Applications*. Morgan Kaufmann/Elsevier.

I. Blank. 1952. Factors which influence the water content of the stratum corneum. *J. Investigat. Dermatol.* 18, 6, 433–440.

W. G. Bruls and J. Van Der Leun. 1984. Forward scattering properties of human epidermal layers. *Photochem. Photobiol.* 40, 2, 231–242.

W. Butler. 1964. Absorption spectroscopy in vivo: Theory and application. *Ann. Rev. Plant Phys.* 15, 451–470.

P. G. Cavalcanti, J. Scharcanski, and G. V. G. Baranoski. 2013. A two-stage approach for discriminating melanocytic skin lesions using standard cameras. *Expert. Syst. Appl.* 40, 10, 4054–4064.

M. Chedekel. 1995. Photophysics and photochemistry of melanin. In *Melanin: Its Role in Human Photoprotection,* M. C. L. Zeise and T. Fitzpatrick, Eds., Valdenmar, 11–22.

B. Chen, K. Stamnes, and J. Stamnes. 2001. Validity of the diffusion approximation in bio-optical imaging. *Appl. Optics* 40, 34, 6356–6336.

T. F. Chen, G. V. G. Baranoski, B. W. Kimmel, and E. Miranda. 2014. Supplementary data for the hyperspectral modeling of skin appearance. NPSG, University of Waterloo, Canada.

C. Cooksey and D. Allen. 2013. Reflectance measurements of human skin from the ultraviolet to the shortwave infrared (250 nm to 2500 nm). In *Proceedings of the SPIE Conference on Active and Passive Signatures (SPIE'13).* Vol. 8734.

K. V. De Graaff. 1995. *Human Anatomy*, 4th Ed. W. C. Brown Publishers.

E. D'eon and G. Irving. 2011. A quantized-diffusion model for rendering translucent materials. *ACM Trans. Graph.* 30, 4, 56:1–13.

C. Donner and H. W. Jensen. 2006. A spectral bssrdf for shading human skin. In *Proceedings of the 17th Eurographics Workshop on Rendering Techniques (EGSR'06).* 409–418.

C. Donner, T. Weyrich, E. D'eon, R. Ramamoorthi, and S. Rusinkiewicz. 2008. A layered, heterogeneous reflectance model for acquiring and rendering human skin. *ACM Trans. Graph.* 27, 5, 140:1–12.

A. Doronin and I. Meglinski. 2011. Online object oriented monte carlo computational tool for needs of the biomedical optics. *Biomed. Optics Express* 2, 9, 2461–2469.

J. Dorsey, H. Rushmeier, and F. Sillion. 2007. *Digital Modeling of Material Appearance*. Morgan Kaufmann/Elsevier, Burlington, MA.

C. Fredembach, N. Barbuscla, and S. Susstrunk. 2009. Combining visible and near-infrared images for realistic skin smoothing. In *Proceedings of the 17th Color and Imaging Conference (CIC'09).* 242–247.

M. Fuchs, V. Blanz, H. Lensch, and H. Seidel. 2005. Reflectance from images: A model-based approach for human faces. *IEEE Trans. Visual. Comput. Graph.* 11, 3, 296–305.

J. Fulton. 1997. Utilizing the ultraviolet (uv detect) camera to enhance the appearance of photodamage and other skin conditions. *Dermatol. Surgery* 23, 163–169.

A. Ghosh, T. Hawkins, P. Peers, S. Frederiksen, and P. Debevec. 2008. Practical modeling and acquisition of layered facial reflectance. *ACM Trans. Graph.* 27, 5, 139:1–10.

D. Greenberg, J. Arvo, E. Lafortune, K. Torrance, J. Ferwerda, B. Walter, B. Trumbore, P. Shirley, S. Pattanaik, and S. Foo. 1997. A framework for realistic image synthesis. In *Proceedings of the 24th Annual Conference on Computer Graphics and Interactive Techniques (SIGGRAPH'97).* 477–494.

D. Hamby. 1994. A review of techniques for parameter sensitivity analysis of environmental models. *Environ. Monitor. Assess.* 32, 2, 135–154.

D. Hamby. 1995. A comparison of sensitivity analysis techniques. *Health Phys.* 68, 195–204.

P. Hanrahan and W. Krueger. 1993. Reflection from layered surfaces due to subsurface scattering. In *Proceedings of the 20th Annual Conference on Computer Graphics and Interactive Techniques (SIGGRAPH'93).* 165–174.

M. Hansen, G. Atkinson, L. Smith, and M. Smith. 2010. 3D face reconstructions from photometric stereo using near infrared and visible light. *Comput. Vis. Image Understand.* 114, 942–951.

A. Hennessy, C. Oh, B. Diffey, K. Wakamatsu, S. Ito, and J. Rees. 2005. Eumelanin and pheomelanin concentrations in human epidermis before and after uvb irradiation. *Pigment Cell Res.* 18, 220–223.

A. Hielscher, S. Jacques, L. Wang, and F. Tittel. 1995. The influence of boundary conditions on the accuracy of diffusion theory in time-resolved reflectance spectroscopy of biological tissues. *Phys. Med. Biol.* 40, 1957–1975.

R. Hunter and R. Harold. 1987. *The Measurement of Appearance*, 2nd ed. John Wiley and Sons.

T. Igarashi, K. Nishino, and S. K. Nayar. 2007. The appearance of human skin: A survey. *Foundat. Trends. Comput. Graph. Vis.* 3, 1, 1–95.

S. L. Jacques. 1996. Origins of tissue optical properties in the uva, visible, and nir regions. *OSA TOPS Adv. Optical Imag. Photon Migrat.* 2, 364–369.

S. L. Jacques, C. A. Alter, and S. A. Prahl. 1987. Angular dependence of HeNe laser light scattering by human dermis. *Lasers Life Sci.* 1, 309–333.

J. Jacquez, J. Huss, W. Mckeehan, J. Dimitroff, and H. Kuppenhein. 1955a. Spectral reflectance of human skin in the region 0.7-2.6 μ. *J. Appl. Physiol.* 8, 297–299.

J. Jacquez, J. Huss, W. Mckeehan, J. Dimitroff, and H. Kuppenhein. 1955b. Spectral reflectance of human skin in the region 235–700 mμ. *J. Appl. Physiol.* 8, 212–214.

J. Jimenez, T. Scully, N. Barbosa, C. Donner, X. Alvarez, T. Vieira, P. Matts, V. Orvalho, D. Gutierrez, and T. Weyrich. 2010. A practical appearance model for dynamic facial color. *ACM Trans. Graph.* 29, 6, 141:1–10.

M. H. Kim, T. A. Harvey, D. S. Kittle, H. Rushmeier, J. Dorsey, R. Prum, and D. Brady. 2012. 3D Imaging spectroscopy for measuring hyperspectral patterns on solid objects. *ACM Trans. Graph.* 31, 4, 38:1–11.

B. W. Kimmel and G. V. G. Baranoski. 2007. A novel approach for simulating light interaction with particulate materials: Application to the modeling of sand spectral properties. *Optics Express* 15, 15, 9755–9777.

N. Kollias, R. M. Sayre, L. Zeise, and M. R. Chedekel. 1991. Photoprotection by melanin. *J. Photochem. Photobiol. B9*, 2, 135–60.

A. Krishnaswamy and G. V. G. Baranoski. 2004a. A biophysically-based spectral model of light interaction with human skin. *Comput. Graph. Forum* 23, 3, 331–340.

A. Krishnaswamy and G. V. G. Baranoski. 2004b. Combining a shared-memory high performance computer and a heterogeneous cluster for the simulation of light interaction with human skin. In *Proceedings of the 16th International Symposium on Computer Architecture and High Performance Computing (SBAC-PAD'04).* P. N. J. Gaudiot, M. L. Pilla, and S. Song, Eds, IEEE Computer Society, 166–171.

P. Latimer. 1984. A wave-optics effect which enhances light absorption by chlorophyll in vivo. *Photochem. Photobiol.* 40, 2, 193–199.

T. S. Lister. 2013. Simulating the color of port wine stain skin. Ph.D. thesis, University of Southampton, UK http://eprints.soton.ac.uk/352088/1.hasCoversheetVersion/Lister.pdf.

H. Mahler, J. Kulik, F. Gibbons, M. Gerrad, and J. Harrel. 2003. Effects of appearance-based interventions on sun protection intentions and self-reported behaviors. *Health Psychol.* 22, 2, 199–209.

S. Marschner, S. H. Westin, E. Lafortune, K. Torrance, and D. Greenberg. 1999. Reflectance measurements of human skin. Tech. rep. PCG-99-2, Program of Computer Graphics, Cornell University.

E. J. Mccartney. 1976. *Optics of the Atmosphere: Scattering by Molecules and Particles*. John Wiley and Sons, New York.

S. Merillou and D. Ghazanfarpour. 2008. A survey of aging and weathering phenomena in computer graphics. *Comput. Graph.* 32, 2, 159–174.

Natural Phenomena Simulation Group (NPSG). 2014. Run hylios online. School of Computer Science, University of Waterloo, Ontario, Canada. http://www.npsg.uwaterloo.ca/models/hylios.php.

C. Ng and L. Li. 2001. A multi-layered reflection model of natural human skin. In *Proceedings of the Computer Graphics International Conference (CGI'01).* 249–256.

F. Nicodemus, J. Richmond, J. Hsia, I. Ginsberg, and T. Limperis. 1992. Geometrical considerations and nomenclature for reflectance. In *Physics-Based Vision Principles and Practice: Radiometry*, L. Wolff, S. Shafer, and G. Healey, Eds. Jones and Bartlett, Boston, 94–145.

K. Nielsen, L. Zhao, J. Stamnes, K. Stamnes, and J. Moan. 2004. Reflectance spectra of pigmented and nonpigmented skin in the uv spectral region. *Photochem. Photobiol.* 80, 450–455.

K. P. Nielsen, L. Zhao, J. J. Stamnes, K. Stamnes, and J. Moan. 2006. The importance of the depth distribution of melanin in skin for DNA protection and other photobiological processes. *J. Photochem. Photobio. B.* 82, 3, 194–198.

A. S. Nunez. 2009. A physical model of human skin and its application for search and rescue. Ph.D. thesis, Air Force Institute of Technology, Wright-Patterson Air Force Base, Ohio.

R. L. Olson, J. Gaylor, and M. A. Everett. 1973. Skin color, melanin, and erythema. *Arch. Dermatol.* 108, 4, 541–544.

M. Pathak. 1995. Functions of melanin and protection by melanin. In *Melanin: Its Role in Human Photoprotection,* M. C. L. Zeise and T. Fitzpatrick, Eds, Valdenmar, 125–134.

S. Prahl. 1988. Light transport in tissue. Ph.D. thesis, The University of Texas at Austin. http://omlc.org/∼prahl/pubs/pdf/prahl88.pdf.

D. Sandidge. 2009. *Digital Infrared Photography Photo Workshop*. Wiley.

P. Schroeder, J. Haendeler, and J. Krutmann. 2008. The role of infrared radiation in photoaging of skin. *Experimen. Gerontol.* 43, 629–632.

J. Stam. 2001. An illumination model for a skin layer bounded by rough surfaces. In *Proceedings of the 12th Eurographics Workshop on Rendering Techniques (Eurographics'01).* Springer, 39–52.

M. Stone. 2003. *A Field Guide to Digital Color*. AK Peters, Natick, MA.

G. Szabo, A. Gerald, M. Pathak, and T. B. Fitzpatrick. 1969. Racial differences in the fate of melanosomes in human epidermis. *Nature* 222, 5198, 1081–1082.

T. S. Trowbridge and K. P. Reitz. 1975. Average irregularity representation of a rough surface for ray reflection. *J. Optical Soc. Amer.* 65, 5, 531–536.

N. Tsumura, M. Kawabuchi, H. Haneishi, and Y. Miyabe. 2000. Mapping pigmentation in human skin by multi- visible-spectral imaging by inverse optical scattering technique. In *Proceedings of the 8th IS&T/SID Color Imaging Conference (CIC'00).* 81–84.

V. Tuchin. 2007. *Tissue Optics: Light Scattering Methods and Instruments for Medical Diagnosis*. SPIE.

M. Vrhel, R. Gershon, and L. Iwan. 1994. Measurement and analysis of object reflectance spectra. *Color Res. Appl.* 19, 1, 4–9.

L. Wang, S. Jacques, and L. Zheng. 1995. MCML – Monte Carlo modelling of light transport in multi-layered tissues. *Comput. Methods Prog. Biomed.* 47, 131–146.

T. Weyrich, W. Matusik, H. Pfister, B. Bickel, C. Donner, C. Tu, J. Mcandless, J. Lee, A. Ngan, H. W. Jensen, and M. Gross. 2006. Analysis of human faces using a measurement-based skin reflectance model. In *Proceedings of the 33rd International Conference and Exhibition on Computer Graphics and Interactive Techniques (SIGGRAPH'06).* ACM Press, New York, 1013–1024.

M. Yang, V. Tuchin, and A. Yaroslavsky. 2009. Principles of light-skin interactions. In *Light-Based Therapies for Skin of Color*, E. Baron, Ed., Springer, 1–44.

D. Yim, G. V. G. Baranoski, B. W. Kimmel, T. F. Chen, and E. Miranda. 2012. A cell-based light interaction model for human blood. *Comput. Graph. Forum* 31, 2, 845–854.

A. R. Young. 1997. Chromophores in human skin. *Phys. Med. Biol.* 42, 5, 789.

Received October 2014; accepted December 2014